Earth and Planetary Science Letters 619 (2023) 118301

Contents lists available at ScienceDirect

Earth and Planetary Science Letters

journal homepage: www.elsevier.com/locate/epsl

The nickel output to abyssal pelagic manganese oxides: A balanced elemental and isotope budget for the oceans

Sarah Fleischmann [a,*], Jianghui Du [a], Aditi Chatterjee [a], James McManus [b], Sridhar D. Iyer [c], Ankeeta Amonkar [d], Derek Vance [a]

[a] Institute of Geochemistry and Petrology, Department of Earth Sciences, ETH Zürich, Clausiusstrasse 25, 8092 Zürich, Switzerland
[b] Bigelow Laboratory for Ocean Sciences, East Boothbay, ME, 04544, USA
[c] CSIR-National Institute for Oceanography, Dona Paula, Goa, 403 004, India
[d] Dnyanprassarak Mandal's College and Research Centre, Mapusa, Goa, 403507, India

ARTICLE INFO

Article history:
Received 28 February 2023
Received in revised form 26 June 2023
Accepted 30 June 2023
Available online xxxx
Editor: L. Coogan

Keywords:
nickel
Ni isotopes
marine sediments
manganese oxide sink
oceanic mass balance

ABSTRACT

The development of nickel isotopes as a chemical tracer of past ocean environments requires a sound understanding of the modern oceanic budget. Our current understanding of this budget implies a large elemental and isotope imbalance between inputs to and outputs from the dissolved pool of the ocean. This imbalance is mainly caused by the dominant oxic sink of Ni to Mn oxide-rich sediments. Though the Ni isotope composition of Fe-Mn crusts has previously been used as proxy for the Ni isotope composition of these sediments, crusts and nodules represent a very small part of the total Mn oxide output. Instead, Mn oxide microparticle supply to pelagic and hemi-pelagic sediments dominates the removal of Mn to sediments, but there are very few isotope data for such samples. Here we present the first extensive Ni concentration and isotope dataset from fully oxic Mn-rich pelagic sediments, from 6 different sites across the open Pacific and 10 closely-spaced sites in the Indian Ocean. We also present data for one hemi-pelagic site representing a suboxic setting on the California Margin. Abyssal Pacific and Indian Ocean sediments have a Ni/Mn ratio of 0.02 (similar to Fe-Mn crusts) and their authigenic Ni is isotopically lighter (δ^{60}Ni = +0.26 to +1.08‰) than seawater (+1.33‰) and crusts (+1.55±0.38‰). Data presented here for organic carbon-rich suboxic sediments of the Californian margin have lower Ni/Mn ratios (0.004 to 0.014 for the oxic top of the core, where Mn oxide is present in abundance) and even lighter authigenic Ni isotope compositions (δ^{60}Ni = -0.08±0.11‰).

We show that the Ni isotopes of nearly all Mn-rich sediments and deposits analysed to date, including the new data presented here, are correlated with Co/Mn ratios, suggesting that both are controlled by accumulation rate, progressive incorporation of Ni into the metal oxide structure and isotopic re-equilibration between the solid and aqueous phase. At sites where sediments are diagenetically processed, such as the California Margin, differential diagenetic remobilisation of Mn, Ni and Co cause deviations from this correlation. We present a new mass balance calculation that recognises the importance of scavenging of oceanic Ni to Mn oxide-rich proximal hydrothermal sediments, with low Ni/Mn and light isotope compositions. The mass balance produces a budget that can be simultaneously balanced for both amounts and isotope compositions of Ni. This result provides a strong basis for the application of Ni isotopes as records of the evolution of the metal sink from the oxic oceans through Earth history.

1. Introduction

Nickel is one of a number of important bio-essential trace metals in the ocean. As such, it shows concentration-depth profiles that are qualitatively similar to those of the major nutrients, such as phosphate and silica, and to other bio-essential metals, such as Fe and Zn (e.g., Sclater et al., 1976; Bruland, 1980). Among the enzymatic roles of Ni, it is an essential component of urease, which is utilised by phytoplankton to recycle urea back to bio-available ammonia (Ragsdale, 2009). In addition, Ni superoxide dismutase and Ni-Fe hydrogenases are important for nitrogen fixation by cyanobacteria and other prokaryotes, and is key to the production

* Corresponding author.
E-mail address: sarah.fleischmann@erdw.ethz.ch (S. Fleischmann).

https://doi.org/10.1016/j.epsl.2023.118301

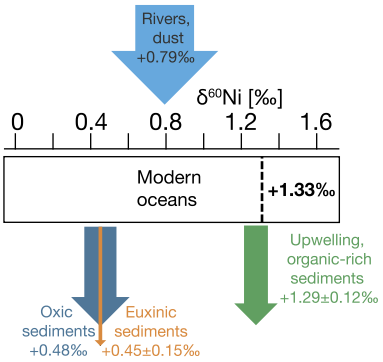

Fig. 1. Inputs (from sources external to the oceans) and net (permanent) outputs from the ocean of Ni and its isotopes. The thickness of the arrows denotes the approximate sizes of the combined sources and each sink. The Ni isotope composition of deep seawater δ^{60}Ni = 1.33±0.13‰ (Lemaitre et al., 2022) is indicated by the black, dashed line. The published constraints on the size and isotope composition (δ^{60}Ni, the parts per thousand deviation of the ^{60}Ni/^{58}Ni ratio from NIST SRM986) of the sources and sinks in this diagram are detailed in the Supplementary Information. Briefly, those of the riverine and dust inputs are from Cameron and Vance (2014). The upwelling margin sink is based on original data from Peru in Ciscato et al. (2018), updated with recent data for Namibia (He et al., 2023). The small euxinic sink is based on data from the Black Sea (Vance et al., 2016). The size and isotope composition of the oxic sink is calculated assuming elemental and isotope balance between the inputs and the permanent outputs, yielding a Ni flux of 2.2x10^8 mol yr^{-1} and a δ^{60}Ni of +0.48‰ (see text and Supplementary Information for further details).

of methane (Ragsdale, 2009), making this element and its isotopes a potential tracer for methanogenesis (Cameron et al., 2009).

A number of recent and older studies have investigated the behaviour of Ni in the photic zone of the modern ocean, in particular the degree to which the photic zone pool of Ni is bioavailable (e.g., Mackey et al., 2002; Archer et al., 2020), and to what extent upper ocean Ni abundances are controlled by nitrogen metabolism or removal by scavenging (e.g., Archer et al., 2020; Lemaitre et al., 2022; John et al., 2022). Here, we focus on the whole ocean dissolved Ni reservoir, and the extent to which Ni's stable isotope system can clarify and quantify whole ocean sources and sinks. Ultimately, this mass balance determines the oceanic dissolved inventory that is available for biological uptake. Moreover, contrasting isotope signatures associated with redox-controlled sinks from the oceanic dissolved pool can help track the history of the ocean's oxidation-reduction potential (e.g., Wang et al., 2019).

Recent attention has centred on the isotope composition of the standing pool of Ni in the modern oceans, as controlled by inputs from outside the ocean, outputs to sediment, and potential back fluxes from sediment (e.g., Ciscato et al., 2018; Little et al., 2020; Gueguen and Rouxel, 2021). Here our emphasis is on a slightly different but related issue: the steady-state balance between the inputs and the net (permanent) outputs, as governed by two simple relationships:

$$\sum F_{in} = \sum F_{out} \quad (1)$$

$$\sum F_{in}\delta_{in} = \sum F_{out}\delta_{out} \quad (2)$$

where $F_{in,out}$ are the sizes of the inputs and output fluxes in mol yr^{-1}, and $\delta_{in,out}$ are their isotope compositions (δ^{60}Ni, as defined in the caption to Fig. 1). Our current understanding of this mass balance for Ni and its isotopes is summarised in Fig. 1, for which the constraints and their literature sources are discussed in detail in the Supplementary Information. Rivers dominate the input, with a minor contribution from dust. Nickel concentrations in hydrothermal fluids imply a dissolved source to the oceans that is only a few percent of the riverine source (see Supplementary Information for details). The oceanic sink of Ni is partitioned into three main permanent sedimentary outputs (Fig. 1, Supplementary Information). The quantitatively important sink via uptake into cells in the photic zone and transfer to organic matter-rich sediments (e.g., Böning et al., 2012, 2015; Plass et al., 2021) beneath modern upwelling zones leads to a sink that is isotopically identical to seawater, as evidenced by authigenic δ^{60}Ni in such sediments of +1.29±0.12‰ (Ciscato et al., 2018; He et al., 2023). A second and much smaller sink has, so far, only been studied in the Black Sea (Vance et al., 2016), where isotopically light Ni (δ^{60}Ni ∼ 0.45‰) is sequestered to euxinic sediments in the sulphidic deep basin.

The third sink, deposition in Mn oxide-rich sediment, is the largest in terms of Ni output and the least well understood, both from the perspective of size and isotope composition. Nickel has a great affinity for particulate Mn oxide (e.g., Sawlan and Murray, 1983; Koschinsky and Halbach, 1995), to which it both sorbs and into which it is structurally incorporated (e.g., Peacock and Sherman, 2007; Peacock, 2009). In Fig. 1, the size and isotope composition of this sink are calculated assuming long-term steady state (equations (1) and (2), and using data for the other sources and sinks), yielding a size of around 2.2x10^8 mol yr^{-1} and δ^{60}Ni of around +0.48‰. There are two major issues with the comparison of this steady-state calculation with observations in the physical manifestation of this output, oxic marine sediments. First-order estimates of metal outputs to the Mn oxide sink are conventionally obtained using the global Mn output and metal/Mn ratios in Mn-rich sediments (e.g., Rehkämper and Nielsen, 2004; Scott et al., 2008; Cameron and Vance, 2014). Nickel and Mn abundances are well-correlated in Fe-Mn crusts, at a Ni/Mn ratio of about 0.02 g/g (data compiled in Manheim and Lane-Bostwick, 1989). This Ni/Mn ratio, combined with a global net output of Mn to oxic sediments of up to 1.1x10^{11} mol yr^{-1} (e.g., van Hulten et al., 2017), implies a Ni output of up to 2.1x10^9 mol yr^{-1}, an order of magnitude more than the steady-state calculation. Secondly, the observed range of δ^{60}Ni in Mn oxide-rich marine sediments, at -0.81 to +2.47‰ (Gall et al., 2013; Gueguen et al., 2016, 2021; Little et al., 2020; Gueguen and Rouxel, 2021), covers the entire range of terrestrial samples measured to date (Saunders et al., 2020).

The assumption that the high Ni/Mn ratio of Fe-Mn crusts and their heavy Ni isotope composition are representative of the initial output of Ni to oxic sediments has led previous studies (Ciscato et al., 2018; Little et al., 2020; Gueguen and Rouxel, 2021) to postulate a large and heavy back-flux from sediment, driven either by mineralogical transformations or redox cycling. However, a recent budgetary exercise (Uramoto et al., 2019) suggests that Fe-Mn crusts and nodules represent only 0.1% of the total pelagic Mn output from the oceanic dissolved pool, so that dispersed Mn oxide particulates are overwhelmingly dominant. Given this dominance, there is a pressing need for further systematic studies of Ni and its isotopes associated with dispersed Mn oxides in marine sediments, as opposed to nodules and crusts. The existing data (Little et al., 2020; Gueguen and Rouxel, 2021) come from very few study sites, which makes it difficult to estimate average Ni isotope values for the Ni sink to pelagic sediments via Mn oxide. Moreover, the precise processes operating in the water column and beneath the sediment-water interface, which set the permanent Ni isotope composition of this dominant sink, need to be better understood if Ni isotopes are to be useful to the study of Earth history. Here, we present new element concentration and Ni isotope data from Mn-rich pelagic sediments from different sites at different depths across the Pacific and Indian oceans. The new data, as well as our analysis of them in terms of sedimentary settings and the oceanic Mn budget, resolve the mass balance issues highlighted above.

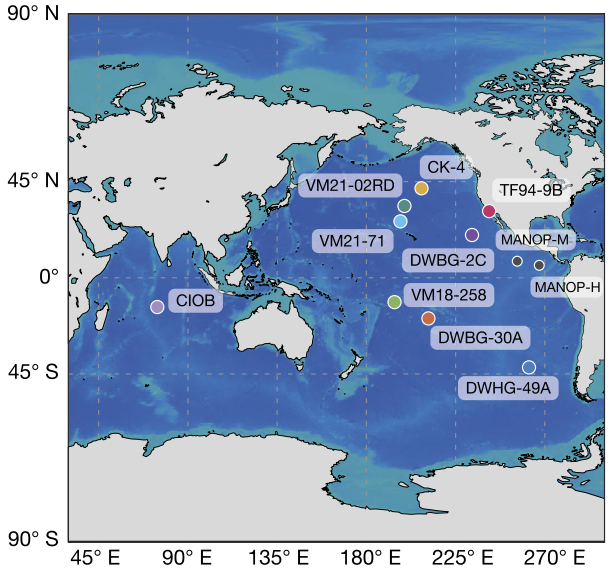

Fig. 2. Locations of the studied sample sites. Note that those in the Indian ocean are located very close to each other, and are represented by a single point on this map.

2. Sample provenance

The samples investigated here come from 8 different sites across the Pacific and from 10 closely-spaced sites in the Indian ocean (Fig. 2).

The open Pacific Ocean sediment samples are all pelagic, deep-sea sediments with the exception of one manganese nodule (VM21-02RD) and come from water depths of 4359-5860 metres. Sediment samples from site DWHG-49A, DWBG-30A, DWBG-2C were assembled from the Scripps Institution of Oceanography Collection and samples from sites VM18-258, VM21-71 and VM21-02RD from the Lamont Doherty Collection. These cores were all sampled during cruises in the late 1950s to early 1960s. They have already been described and analysed for various element concentrations by Krishnaswami (1976). The Indian Ocean samples were collected using Okean grabs (depth of penetration 50 cm), box-core (40 cm depth) and a Peterson grab and are from water depths of 4750-5390 metres. The origin and significance of sediment components at these sites are discussed in Amonkar and Iyer (2021). Bottom water O_2 concentrations for these precise open ocean locations are not available, but the nearest stations from the Global Ocean Data Analysis Project (Bottle Data, version 2.2022, Lauvset et al., 2022) suggest values that are always greater than 140 µmol/kg.

Samples from site TF94-9B (water depth of 2053 m) were taken in the course of the "TEFLOM" expedition in 1994, in the southern California Borderland Basin area. This site has been subject to previous studies that explored diagenetic fluxes from continental margin sediments (Berelson et al., 1996; McManus et al., 1997, 2012) and corresponds to the core "SC-1" in these publications. Bottom water oxygen is 52 µM, and the calculated oxygen penetration depth is 1.28 cm (Berelson et al., 1996).

3. Methods summary

The analytical methods used here have been detailed in previous publications (Vance et al., 2016; Archer et al., 2020). A short summary is given here, with more details in the Supplementary Information.

Concentrations of selected elements were measured on a Thermo Scientific Element XR at ETH Zürich, with concentrations obtained by comparison to in-house primary standards. For most elements, repeat analyses of the reference materials SLRS-6 (river water) and SGR-1 (shale) were used to monitor accuracy and reproducibility. For the elements of interest here, reproducibility is 8-12% (95% confidence), though for Al it is estimated as 15%. Elemental concentrations have been adjusted to take account of minor inaccuracies in results for the reference standards. For REE measurements, the reference material NASS-5 was used to determine accuracy and reproducibility, yielding long-term reducibility of 5-8% for all REE and accuracy better than the 1-sigma ranges of reported values in the literature. We also add REE and Co data for some of the MANOP samples analysed for Ni isotopes in Little et al. (2020).

The isotope compositions of purified Ni fractions were determined using a Thermo Scientific Neptune Plus MC-ICP-MS at ETH Zürich. Nickel isotopic compositions are reported in the standard delta notation relative to the NIST SRM986 standard:

$$\delta^{60}Ni\,(‰) = \left[\frac{\left(\frac{60Ni}{58Ni}\right)_{Sample}}{\left(\frac{60Ni}{58Ni}\right)_{SRM986}} - 1\right] \times 1000 \qquad (3)$$

Long-term reproducibility of Ni isotope analyses was assessed via repeat analyses of two secondary standards, USGS NodA1 and NodP1. Over the past 7 years, these two standards have yielded δ^{60}Ni = +1.04 ± 0.07‰ (2 sigma, n = 474) and +0.34 ± 0.08‰ (2 sigma, n = 650), respectively. The uncertainty of ± 0.08‰ is plotted in the figures.

All the bulk sediments studied here are enriched in trace metals over and above the upper continental crust (e.g., Rudnick and Gao, 2014), but it is the authigenic metal concentrations that are important for this investigation, and corrections for detrital contributions to the bulk sample have been applied. These corrections were done as described in Ciscato et al. (2018), with specific details given in the Supplementary Information.

4. Results

Metal abundances, Ni isotope compositions, REE abundances and total organic carbon (TOC) measurements are presented in Tables S1-S4 in the Supplementary Information.

4.1. Open ocean sediments from the Pacific and Indian Ocean

4.1.1. TOC and elemental abundances

The TOC content of all the bulk open Pacific and Indian Ocean samples is low, with maximum values of 0.3 wt% (Table S1). Bulk Mn concentrations, ranging from 0.16 to 2.5% (Table S1), differ from site to site, but show only minor variation versus core depth within the top 20-60 cm at any one site. Bulk Ni concentrations range from 84 to 597 ppm (Table S1) and, like Mn, vary across sites but are rather homogeneous with core depth at the same site. All trace metals are enriched relative to detrital abundances, with bulk Mn/Al ratios 2-161 times the UCC (Rudnick and Gao, 2014) and Ni/Al ratios 6-221 times the Ni/Al ratio of detrital material (Böning et al., 2012). Thus, the authigenic fraction (Fig. 3) dominates bulk sediment concentrations. Authigenic Ni and Mn concentrations in the sediments are highest at site DWHG-49A and lowest at site CK-4 and generally correlate in all cores (see Fig. 3). The Mn nodule from site VM21-02RD is extremely enriched in Ni (Table S1, 4600 ppm, Ni/Al = 1145 times detrital) and Mn (13.5% = 598 times the UCC) compared to the Mn-rich sediments.

The REE patterns of the samples are shown normalised to North Pacific Deep Water (NPDW, Nozaki et al., 1999) in Fig. S4A and in terms of the solid-solution partition coefficient, after further normalisation to Nd, in Fig. S4B. The REE patterns of the labile fractions of pelagic particles from the deep ocean (>1000 m), as well

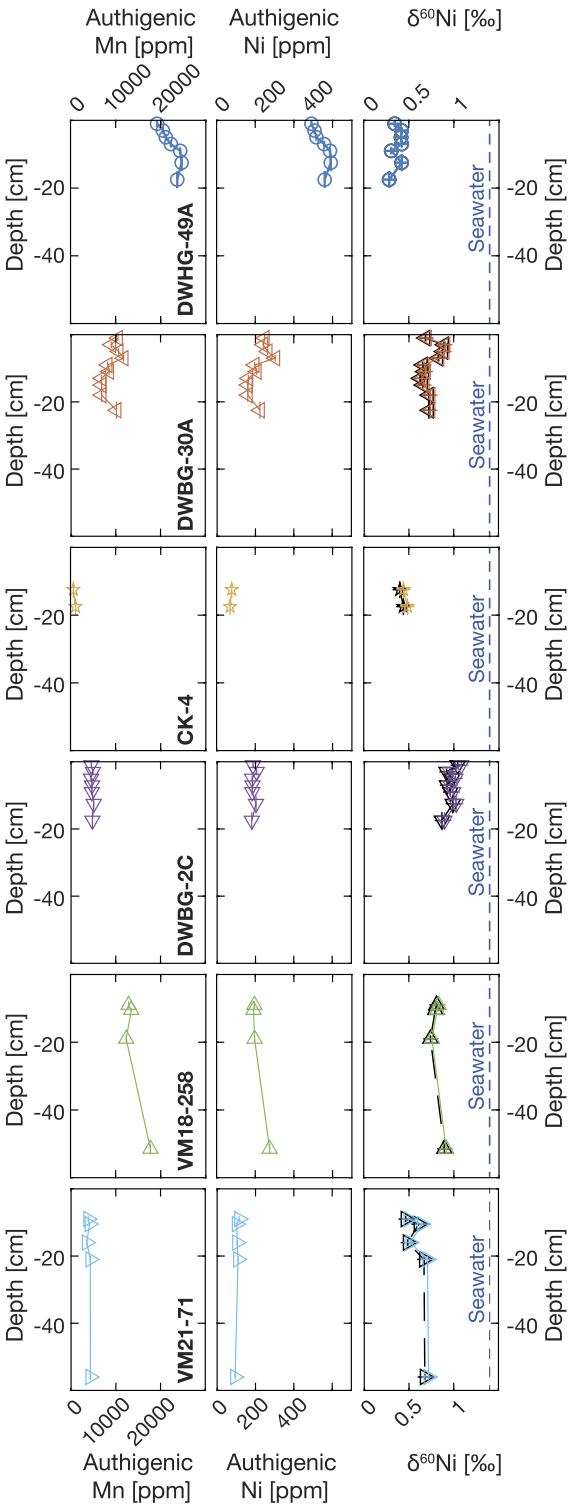

Fig. 3. Authigenic Mn, authigenic Ni and Ni isotopes vs. depth beneath the sediment-water interface for cores from the abyssal Pacific Ocean. The black, dashed lines in the Ni isotope plots represent values without detrital correction, while the coloured symbols and continuous lines are authigenic Ni isotope values. The blue, dashed line is the Ni isotope composition of deep seawater δ^{60}Ni = 1.33±0.13‰, beneath 500 m, data compiled in Lemaitre et al. (2022). The roughly 20% drop in authigenic concentrations of all elements at the top of core DWHG-49A (see also Table S1) is due to dilution by calcite, as indicated by bulk Ca concentrations that are double those further down the core.

as hydrothermal deposits from Loihi, are also plotted for comparison (Fig. S4B). Overall, Mn-rich sediments, Mn nodules and pelagic particles have a similar pattern: an enrichment of light and middle REE relative to heavy REE, a distinct positive Ce anomaly and a slight negative Y anomaly (Fig. S4B). The hydrothermal deposits also share this pattern, but with an additional small positive Eu anomaly (Fig. S4B).

4.1.2. Ni isotopes

Nickel isotopes, expressed as δ^{60}Ni, of the bulk open-ocean Mn-rich sediments range from +0.25 to +1.04‰, while the Mn nodule has a δ^{60}Ni of +0.33‰ (Table S1). Like Mn and Ni concentrations, Ni isotopes vary only slightly with depth at any one site, but are different from site to site (Fig. 3). The Ni isotope compositions of these open ocean samples are heavier than published data for sediments of the MANOP sites of the eastern Pacific (−0.79 to −0.17‰; Little et al., 2020), but lighter than the surfaces of Fe-Mn crusts (+1.55±0.38‰; Gall et al., 2013; Gueguen et al., 2016) and seawater (Fig. 3).

4.2. Suboxic sediments from the eastern Pacific

4.2.1. TOC and elemental abundances

The single core studied here from the California Borderland Basin area, close to the eastern Pacific continental margin (core TF94-9B), exhibits a number of differences from the open ocean samples described above. Firstly, the samples contain at least an order of magnitude more organic carbon, with TOC values of 2.8 to 3.3 wt% (Table S2). Secondly, though all samples are also enriched in Mn (Mn/Al = 2-69 times the UCC), this enrichment is much more variable across the depth range of the core. Thus, bulk Mn concentrations increase sharply in the top 5 centimetres, from 0.23% at 5 cm to 4% at the top, with this sharp increase also reflected in authigenic Mn (Fig. 4). The sediments of core TF94-9B are also enriched in Ni (Ni/Al ratios 11-14 times detrital), with concentrations of 120 to 149 ppm, but Ni concentrations show a much more subtle increase towards the top of the core compared to Mn (Fig. 4). Rare-earth element patterns (Figs. 4A and 4B) for the TF94-9B core, as well as those obtained from the new REE data for the MANOP sites in Little et al. (2020), are similar to those of the open ocean sediments (Fig. S4), particularly when normalised to NPDW.

4.2.2. Ni isotopes

Nickel isotopes (δ^{60}Ni) of the TF94-9B sediments are lighter than the measured open-ocean sediments and significantly lighter than seawater Ni isotope compositions (Fig. 4), ranging from −0.20 to 0.09‰. There is a slight shift to lighter Ni isotope compositions towards the top of the core.

5. Discussion

The isotope compositions of authigenic Ni in modern Mn oxide-rich sediments, including the data presented here, as well as those in recent publications (Gall et al., 2013; Gueguen et al., 2016, 2021; Little et al., 2020; Gueguen and Rouxel, 2021), span a range in δ^{60}Ni of -0.81 to +2.47‰, encompassing almost the entire range of Ni isotope compositions in terrestrial samples measured to date (see data compilation in Saunders et al., 2020). Given the importance of the Mn oxide sink to the oceanic Ni mass balance, there is clearly a need to develop some systematic understanding of this variability. It is this understanding that guides the following discussion, which we focus around three main issues: (1) how the sedimentological and geochemical settings of Mn oxide-rich sediments vary; (2) how these settings control Ni isotope variability; (3) to what extent the relative magnitudes of these different sinks

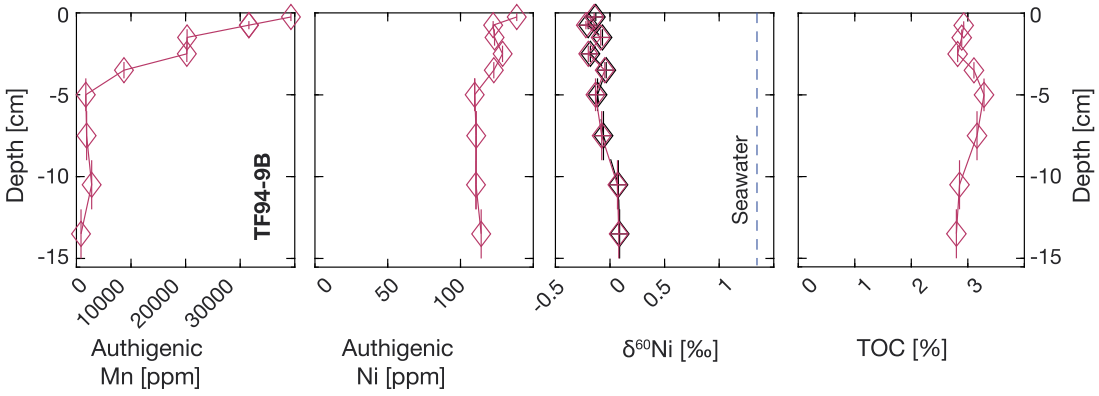

Fig. 4. Authigenic Mn, authigenic Ni, Ni isotopes and TOC vs. depth beneath the sediment-water interface for bulk Pacific margin sediments (site TF94-9B). The black, dashed line in the Ni isotope plot represents values without detrital correction, while the coloured symbols and continuous lines are authigenic Ni isotope values. The blue dashed line is the Ni isotope composition of deep seawater (δ^{60}Ni = 1.33±0.13‰, beneath 500 m, data compiled in Lemaitre et al., 2022). In contrast to the open abyssal Pacific and Indian Ocean samples (Fig. 3), this core from a sub-oxic (manganese reducing) setting shows very significant and systematic changes with depth, including a drop in δ^{60}Ni of 0.3‰ from bottom to top.

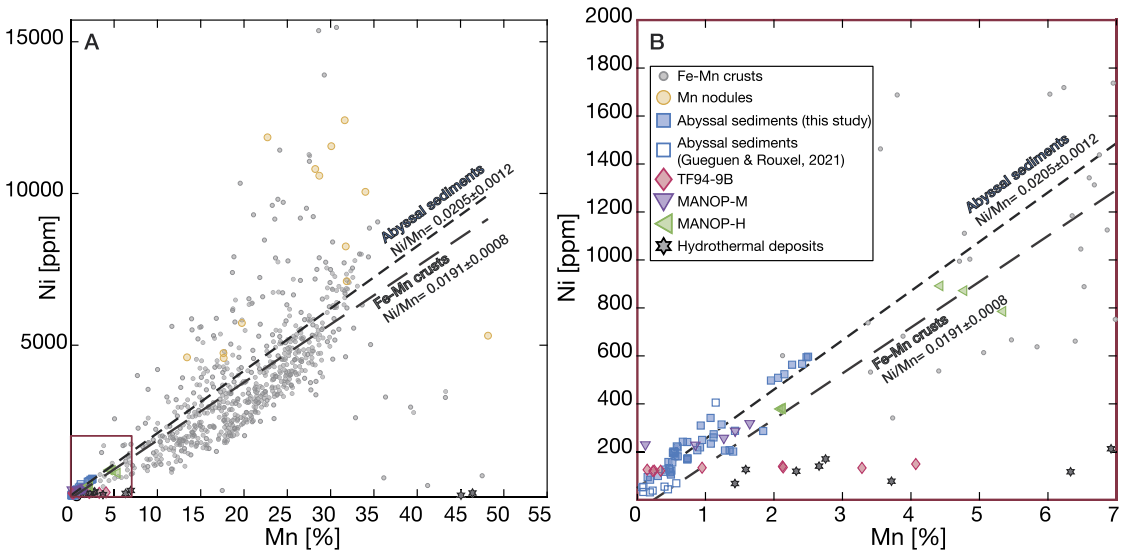

Fig. 5. (A) Bulk Ni [ppm] vs. Mn concentrations [%] for Fe-Mn crusts and nodules and Mn oxide-rich pelagic sediments, from this study and the literature. The slope for abyssal Mn oxide-rich sediments from the Pacific and Indian Ocean (this study) is identical to that for Fe-Mn crusts (data in Manheim and Lane-Bostwick, 1989; Gueguen et al., 2016, 2021); (B) Detail of the bottom left of panel A to better highlight Mn-rich pelagic sediments (this study, Little et al., 2020; Gueguen and Rouxel, 2021) and hydrothermally-influenced deposits (Gueguen et al., 2021). Note the difference between abyssal Pacific and Indian Ocean sediments versus those from the sites TF94-9B and MANOP-M, which derive from a continental margin setting and show a much weaker correlation between Ni and Mn concentrations.

can be quantified to arrive at a more robust mass balance for oceanic Ni and its isotopes that might be useful in paleoceanography.

5.1. Comparative geochemistry of different Mn oxide sinks for Ni

Recent Mn data for sediments of the South Pacific Gyre (Uramoto et al., 2019) have emphasised the dominance of Mn oxide microparticles delivered to pelagic and hemi-pelagic sediments to the oceanic Mn budget, as opposed to Mn crusts and nodules. Thus, while the relatively pure Mn crusts and nodules have been important for characterizing the Ni content and isotope composition of the Mn oxide output generally, they represent only 0.1% of that output (Uramoto et al., 2019). Fig. 5 compares Mn and Ni concentrations for the samples studied here with published data for Fe-Mn crusts, as well as recent data for both Fe-Mn nodules and Mn-rich sediments from studies primarily focused on Ni isotopes (Gueguen et al., 2016, 2021; Little et al., 2020; Gueguen and Rouxel, 2021).

Fig. 5 clearly separates Mn-rich deposits into three groupings. Manheim and Lane-Bostwick (1989) present a large compilation of concentration data for Fe-Mn crusts, which these authors define as “encrustations forming largely on hard substrates … kept free from detrital sedimentation by strong currents, steep slopes, or both.” Most of the Fe-Mn crust data lie on a well-defined array suggesting a Ni/Mn ratio of 0.0191±0.0008 (1 sigma) g/g, consistent with the well-known, strong association of Ni with MnO_2 (e.g., Sawlan and Murray, 1983; Koschinsky and Halbach, 1995). Abyssal Pacific and Indian ocean sediments (this study, Gueguen and Rouxel, 2021) have much lower absolute Mn and Ni concentrations than nodules and crusts, simply due to dilution with material other than the pure metal oxides (Fig. 5B), but the Ni/Mn ratio of these samples is indistinguishable from that for crusts, at 0.0205±0.0012 (1 sigma) g/g. Clearly, the Ni in these samples is dominated by that associated with Mn oxide, and the Ni/Mn ratio is similar to Fe-Mn crusts. Both types of deposit precipitate from seawater and, of the two, Mn microparticles dominate (Uramoto et al., 2019). The Ni and Mn derive from a water column with abun-

dant dissolved O_2 and are delivered to sediments that are poor in particulate organic carbon (Table S1) and whose porewaters are replete in dissolved O_2 (D'Hondt et al., 2015). Mineralogically, these kinds of deposit are dominated by hexagonal birnessite (e.g., Burns and Burns, 1977; Peacock and Sherman, 2007; McMurtry, 2009; Atkins et al., 2016).

Manheim and Lane-Bostwick (1989) and many others (see review in McMurtry, 2009) contrast crusts with "abyssal nodules, which are found lying on or in soft sediments…." The small dataset for Mn nodules (Little et al., 2020; Gueguen et al., 2021) in Fig. 5 hints at a second group with higher Ni/Mn ratio, and the possibility that some of the crusts may also be skewed in that direction. However, a third group of samples from two different kinds of settings show different behaviour from either of the above groups. Firstly, Mn deposits that are clearly hydrothermally influenced, from the Lau Basin and Loihi, show a great deal of variation in Mn concentration at fairly constant Ni concentration. Secondly, the TF94-9B samples studied here show similar characteristics, with Mn ranging from 0.15 to 4% (Table S2) at rather low and relatively invariant Ni concentrations (120-149 ppm). Core TF94-9B is from the suboxic California Margin, where Mn oxide is clearly reductively mobilised at depth and oxidatively re-precipitated in the top 5 cm (Fig. 4). The small dataset for the MANOP sites (Little et al., 2020), also from the California Margin, has characteristics that show some similarities with this latter grouping. These sites also show reductive mobilisation of Mn at depth and re-precipitation near the sediment-water interface (Lyle et al., 1984; Finney et al., 1988). On Fig. 5, MANOP-M shows variation in Mn concentrations across more than an order of magnitude (0.12-1.65%) but Ni concentrations that vary by less than a factor of 1.5 (228-317 ppm). On the other hand, MANOP-H samples lie close to the array for abyssal sediments.

These two different Ni/Mn ratios of oceanic Mn deposits must be determined by three fundamental controls: the Ni/Mn ratio of the fluid from which the solids precipitate, the mineralogy of the solid phase and the mode of incorporation of Ni into the solid mineral phase (sorption versus incorporation). Direct measurements of the Ni/Mn ratios of hydrothermal fluids are scarce, but those available for fast-spreading, basaltic systems that are clearly not influenced by interaction with sediment range from $\leq 1x10^{-5}$ to $2x10^{-4}$ mol/mol (Edmond et al., 1979; Von Damm et al., 1985; Schmidt et al., 2017). Studies of proximal hydrothermal Mn deposits, including those proximal to the East Pacific Rise where hydrothermal fluids are at the low end of this range (e.g., Boström et al., 1973; Kraemer and Schornick, 1974; Corliss et al., 1978; Gueguen et al., 2021), report Ni/Mn ratios of 0.0016±0.0023 (see Supplementary Information for literature sources), 1-2 orders of magnitude higher than hydrothermal fluids. Thus, we concur with the long-held view that, while the Mn in hydrothermal deposits generally is clearly hydrothermal in origin, the Ni and other trace metals these deposits contain are scavenged by the precipitating Mn oxides from seawater (e.g., Elderfield, 1976; McMurtry, 2009; Tagliabue et al., 2018). This conclusion is also consistent with the REE data presented here (Fig. S4, Fig. S5). Hydrothermal sediments from Loihi (Gueguen et al., 2021) share the REE pattern of our abyssal pelagic Mn-rich sediments, except for a slightly positive Eu anomaly (~1.60, much weaker than that of hydrothermal fluid at ~17.3, Fig. S5). Both are similar to the pattern of the labile fractions of pelagic particles, thought to be caused by fractionation due to adsorption of seawater REE onto particulate Mn oxide in the water column (Bertram and Elderfield, 1993; Sholkovitz et al., 1994).

All the California Margin sites are characterised by sediments with high abundances of organic carbon, up to an order of magnitude higher than those of the abyssal sites studied here (Tables S1, S2; Lyle et al., 1984; Finney et al., 1988). At all these sites, reductive dissolution of Mn oxide at depth within the sediment, fuelled by the respiration of this organic carbon (e.g., Lyle et al., 1984; Finney et al., 1988), results in differential diagenetic re-processing of Mn oxides and the associated Ni. For example, re-oxidation near the sediment-water interface of Mn mobilised under reducing conditions at depth and diffusing upwards through porewater, is associated with a barely significant increase in solid-phase Ni concentrations at site TF94-9B (Fig. 4). The same feature characterises Mn and Ni at the MANOP sites (Fig. S6). This suggests that the reduction of Mn oxide at depth releases Ni to pore waters that is not quantitatively trapped when Mn oxide re-precipitates in the oxic zone at the sediment-water interface, resulting in much lower Ni/Mn ratios in the oxidative zone at the top than the reductive zone at the bottom. Porewater data (e.g., Shaw et al., 1990; Heller et al., 2018) from the California Margin and other locations support a diffusive loss of Ni to bottom water, even when Mn oxide is oxidatively re-precipitating at the sediment-water interface. Finally, we note that the relatively high Ni/Mn ratio of diagenetic nodules forming above suboxic sediments (yellow circles in Fig. 5) represents the complement of processes in the sediment, and that they would accrete from the high Ni/Mn fluids that escape the sediment-porewater system.

Aside from the Ni/Mn ratio of the fluids, there may also be a role for mineralogy. Studies of proximal hydrothermal deposits suggest that, in contrast to hydrogenetic Mn deposits, the tectomanganate todorokite is an important, often dominant, mineral phase (e.g., Burns and Burns, 1977; Corliss et al., 1978; McMurtry, 2009). The low Ni/Mn ratio of the hydrothermal deposits in Fig. 5 is, therefore, consistent with the experimental finding that todorokite has lower Ni/Mn ratios than hexagonal birnessite (Atkins et al., 2014, 2016). Tectomanganate minerals like todorokite are also known to occur in suboxic diagenetic settings such as those relevant to the California Margin sites studied here and those in Little et al. (2020). Todorokite is the Mn mineral that forms in environments with the lowest oxidation potential (McMurtry, 2009; Wegorzewski et al., 2020). Though todorokite is generally thought to form as a transformation product of birnessite (e.g., Atkins et al., 2014), it may be the final stable Mn mineral where porewaters become oxidizing enough for dissolved Mn to re-precipitate close to the sediment-water interface. Consistent with the possible importance of todorokite, the Ni/Mn ratio of the Mn oxide at the sediment-water interface in these suboxic settings is less than the 0.02 found for the pelagic abyssal ocean (0.004-0.014 for the California Margin site studied here; Table S2).

5.2. What controls the Ni isotope composition of the different Mn oxide sinks?

A number of recent studies, both observational and experimental, have sought to understand the very large observed range in the Ni isotope compositions of Mn oxide-rich sediments (e.g., Gueguen et al., 2018; Sorensen et al., 2020; Little et al., 2020; Gueguen and Rouxel, 2021). Nickel is both sorbed onto and incorporated into Mn (oxy)hydroxides, particularly hexagonal birnessite (e.g., Peacock and Sherman, 2007; Manceau et al., 2007). In a recent experimental study, Sorensen et al. (2020) found that Ni sorbed to birnessite is isotopically lighter than aqueous Ni ($\Delta^{60/58}Ni_{min\text{-}aq}$=-2.76‰ to -3.35‰). Surface adsorbed Ni may also, with time, be incorporated into vacancy sites to become part of the hexagonal sheet structure (e.g., Peacock, 2009; Kwon et al., 2013; Sorensen et al., 2020). Chen et al. (2022) recently presented experimental results which support the suggestion that incorporated Ni is isotopically heavier than sorbed Ni. In addition, Chen et al. (2022) experimentally transformed a synthetic Ni-Mn oxide analogous to marine birnessite into todorokite and found that the todorokite released isotopically heavy Ni to an aqueous phase during this transformation.

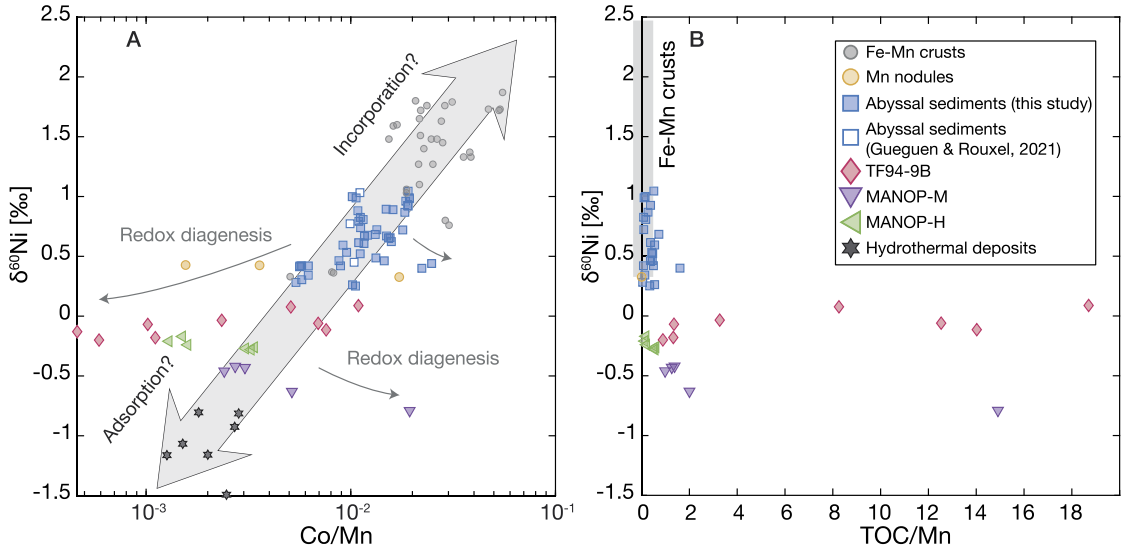

Fig. 6. δ^{60}Ni of different types of Mn oxide-rich sediments from this study and the literature versus: (A) Co/Mn and (B) TOC/Mn. The grey bar in panel B shows the Ni isotope range of Fe-Mn crusts, for these latter, TOC is not available for these samples, but their TOC/Mn must be close to zero. Fe-Mn crusts (Gueguen et al., 2016, 2021) and abyssal sediments (this study and Gueguen and Rouxel, 2021) have the heaviest Ni isotope compositions and Co/Mn ratios, but very low TOC/Mn ratios. The TF94-9B, the MANOP sites (Little et al., 2020) and hydrothermal deposits (Gueguen et al., 2021) are isotopically light with low Co/Mn ratios. The thin arrows in panel A are intended to highlight the fact that Co/Mn ratios at the TF94-9B and MANOP sites are very low at the top of the core (arrow pointing down and left) and higher at the bottom (arrow pointing down and right), which we suggest reflects differential mobilisation of Co and Mn upwards, and differential loss to the water column at the top, in these sub-oxic cores. The TF94-9B and MANOP-M sites also have very high TOC/Mn ratios. Two Lau Basin samples from Gueguen et al. (2021) have not been plotted on Fig. 6A: these samples are unique in that they are from a hydrothermal setting but are also Fe-Mn crusts, with ~50% Mn.

Little et al. (2020) suggested the possibility that the isotope composition of Mn oxide-associated Ni could be modified by post-depositional processes, either by mineral transformations such as that from birnessite to todorokite, or by reductive-oxidative cycles involving manganese oxide dissolution and reprecipitation. As noted earlier, todorokite is rarely found in hydrogenetic ferromanganese crusts, whereas it is generally prevalent in deeply buried nodules (Burns and Burns, 1977; Corliss et al., 1978; Atkins et al., 2016; Heller et al., 2018; Wegorzewski et al., 2020). As also noted earlier, experimental work (Atkins et al., 2016) has demonstrated that during the mineralogical transformation from birnessite to todorokite a substantial proportion of the Ni originally sorbed to birnessite is released into solution, while the remaining solid-associated Ni is adsorbed to todorokite via surface complexation. Little et al. (2020) suggested that the mineral transformation from birnessite to todorokite fractionates Ni isotopes towards lighter compositions, releasing isotopically heavy Ni into porewater (Chen et al., 2022). A second possibility raised by Little et al. (2020) is that the redox cycling of Mn, regardless of mineralogical transformations, could also alter the initial Ni isotope composition of Mn oxide sediments, shifting them towards light isotope values. Specifically, resorption of light Ni on residual or newly precipitating Mn oxide could preferentially sequester the light isotopes (Sorensen et al., 2020) while retaining the heavy isotopes in the pore water to be released to the water column.

We explore the potential impact of the above processes in Fig. 6, which shows the δ^{60}Ni of different types of Mn oxide-rich sediments from this study and the literature versus: A) Co/Mn and B) TOC/Mn. Most of the data on Fig. 6A show clear and systematic co-variation between the Co/Mn ratio, which ranges over 1.5 orders of magnitude, and Ni isotope composition. We hypothesise that none of the sediments along this trend have undergone significant redox-driven diagenetic or mineralogical modification. They all derive from a deep ocean with high bottom water oxygen and, where data are available, lack the significant amounts of organic carbon that could drive redox-related diagenetic processes (Fig. 6B). For the abyssal ocean sediments studied here, we find no variation in authigenic concentrations of Ni and Mn, in the Ni/Mn ratio, or in Ni isotopes, over the analysed depth range (corresponding to around 100-500 kyr given sedimentation rates in Krishnaswami, 1976). Furthermore, these sediments have similar Ni/Mn ratios to Fe-Mn crusts (Fig. 5).

The Co flux to sediments per unit time and area is nearly constant (Halbach et al., 1983), so that the Co concentration in Fe-Mn deposits is inversely related to accumulation rate (e.g., Manheim and Lane-Bostwick, 1988). For example, Fe-Mn crusts (growth rate of <1 to about 10 mm/Myr, Hein et al., 2000) have higher Co/Mn ratios than the abyssal open ocean sediments studies here (sedimentation rate of about 1000 mm/Myr, Krishnaswami, 1976). The MANOP sediments, at the bottom left of the main data array in Fig. 6A accumulate at about 6000 mm/Myr (Finney et al., 1988). We hypothesise that the co-variation between Co/Mn and Ni isotopes defined by the arrow in Fig. 6A is most readily explained by three linked processes: (1) an initial isotope fractionation due to sorption, preferring the light isotope; (2) the progressive structural incorporation of this sorbed Ni, rejecting the light isotope; (3) the availability of a fluid phase to exchange with the solid, taking up the light isotope rejected from the solid during the progressive switch from sorption to structural incorporation. We suggest that it is this latter factor that leads to the correlation on Fig. 6A with accumulation rates; the switch from dominantly sorbed to dominantly structurally incorporated Ni will lead to an isotope shift in the solid if this solid can exchange isotopes with a fluid (see also Sorensen et al., 2020; Chen et al., 2022).

The significant deviations from the main trend on Fig. 6A are represented by the California Margin sediments and Pacific diagenetic Mn nodules. For those for which TOC is available, these samples are also clearly distinguished in Fig. 6B. The samples lying along the main trend in Fig. 6A plot at low TOC/Mn and variable δ^{60}Ni. As above, their low TOC/Mn is consistent with insignificant diagenetic processing and their variable δ^{60}Ni is correlated with Co/Mn and accumulation rates (Fig. 6A). In contrast, the California Margin samples plot at a fairly constant δ^{60}Ni and variable but higher TOC/Mn. Cobalt is well known to diffuse out of reducing sediments (e.g., Tagliabue et al., 2018; Plass et al., 2021), with the latter authors suggesting that Co would remain in the

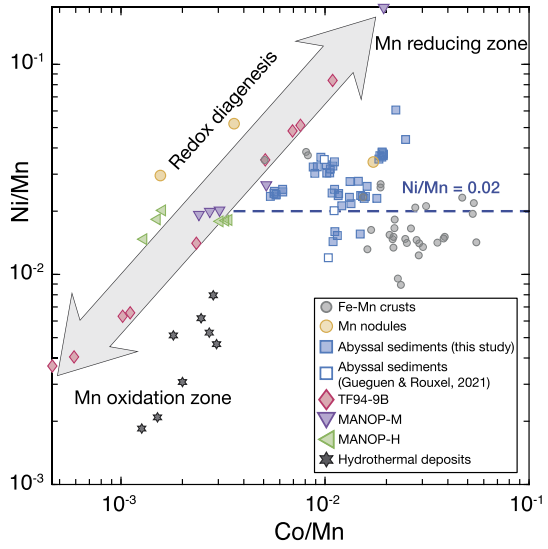

Fig. 7. Ni/Mn versus Co/Mn for the same sample set as in Fig. 6. Sediments from all the California Margin sites lie on a trajectory that differentiates these samples from abyssal pelagic sediments and crusts (around 0.02 g/g), towards low Ni/Mn coupled to low Co/Mn for sediments in the re-oxidation zone at the sediment-water interface and towards high ratios (but at very low absolute Mn concentrations) deeper in the cores where Mn oxide is being reduced. The low ratios at the sediment-water interface are interpreted here as due to non-quantitative sequestration of Ni and Co to the re-precipitating Mn oxide.

aqueous phase while Mn oxidatively re-precipitates close to the sediment-water interface. The pseudo-horizontal displacements indicated by the arrows on Fig. 6A allow for some associated Ni isotope fractionation, but could most simply be due to loss across the sediment-water interface, similarly to that suggested for Ni. This hypothesis is supported by the fact that Ni/Mn and Co/Mn ratios in California Margin sediments are positively correlated (Fig. 7), and that the Mn that re-precipitates oxidatively at the sediment-water interface has the lowest Ni/Mn and Co/Mn ratios, lower for both ratios than pelagic Mn oxides that have not encountered such redox processing (Fig. 7).

Thus, it is *possible* that all the data on Fig. 6A are explained by only two processes: (1) variation in the degree of incorporation of Ni into the birnessite structure and isotopic re-equilibration between the solid and an aqueous phase; (2) fractionation of the Co/Mn ratio by diagenetic re-processing. Though the presence of todorokite may have an impact on the hydrothermal samples at the bottom end of the arrow on Fig. 6A, these samples lie on the same trend as the birnessite-bearing abyssal ocean sediments and crusts at its other end. Indeed, Gueguen et al. (2021) attributed the low Co/Mn ratio of hydrothermal deposits to fast sedimentation rates. On the other hand, we suggest that mineralogy, birnessite versus todorokite, may also play a role. As noted earlier, todorokite is at least present, perhaps dominant, in the hydrothermal samples, and may control the low Ni/Mn ratios of these samples. Todorokite is also likely to be present in suboxic settings and again provides an obvious mechanism to explain the low Ni/Mn ratio in the zone of Mn oxide re-precipitation at the sediment-water interface.

5.3. A new mass balance for oceanic Ni and its isotopes

The preceding discussion suggests a resolution to the mass balance problems highlighted in the introduction: the requirement that the global Mn oxide output of Ni must amount to about 2.2×10^8 mol/yr with δ^{60}Ni of about +0.48‰. Specifically, the sink of Ni from the dissolved pool of the oceans is, in fact, partitioned into three different sinks with different Ni/Mn ratios and Ni isotope compositions. As noted earlier, the abyssal sink is dominated by Mn microparticles exported to pelagic sediments. The Ni/Mn ratio of this sink is around 0.02 g/g (Fig. 5). Its authigenic δ^{60}Ni can be estimated from the samples investigated here (Table S1) and those in Gueguen and Rouxel (2021). Some of the samples in Gueguen and Rouxel (2021) contain substantial detrital Ni so that we have applied a detrital correction, as to our own samples. Using samples only where authigenic Ni dominates (Ni/Al > 10×10^{-4}), the δ^{60}Ni of this first sink = +0.68±0.24‰ (1 SD, n = 44). At the other extreme lies the proximal hydrothermal sink: Ni scavenged from seawater via the precipitation of the very large amounts of hydrothermal Mn. The Ni/Mn ratio of hydrothermally influenced samples ranges from 0.0001 to 0.008, with a mean of 0.0026±0.0024 (1SD, n = 18, Boström et al., 1973; Kraemer and Schornick, 1974; Corliss et al., 1978; Gueguen et al., 2021). The constraints on the δ^{60}Ni of this sink come from the 7 hydrothermal samples from Loihi in Gueguen et al. (2021): -1.06±0.24‰ (1SD). The suboxic California Margin samples (Table S2; Lyle et al., 1984; Finney et al., 1988; Little et al., 2020) are intermediate in both authigenic δ^{60}Ni (-0.25±0.22‰, n=20) and Ni/Mn ratio (0.004-0.025 for the upper oxic levels of the cores, where Mn oxide is up to 20 times more abundant than in the lower levels, see Table S2 and Fig. 4) and potentially complicate a simple mass balance model, but we show below that this sink must be small relative to the other two if the Ni elemental and isotopic mass balance are to be solved simultaneously.

Fig. 8 explores how the size and isotope composition of the global Mn oxide sink varies if partitioned into two different sinks (abyssal pelagic plus suboxic in panel A, and abyssal pelagic plus hydrothermal in B) as a function of the isotopic and geochemical characteristics summarised above. How much Ni is buried globally is a function of the average global Mn burial rate which, in previous models of this general kind, has been taken to be 0.5 $\mu g\,cm^{-2}\,yr^{-1}$ over the 86% of the area of ocean floor that has an oxic sediment-water interface, (e.g., for Mo, Reinhard et al., 2013). A recent model of water column Mn concentrations (van Hulten et al., 2017) suggests inputs to the dissolved pool that are dominated by a hydrothermal source (1.03 out of a total input of 1.09×10^{11} $mol\,yr^{-1}$) and, for steady state, require a global average Mn burial rate of 2 $\mu g\,cm^{-2}\,yr^{-1}$. Though qualitatively consistent with Mn burial rates close to mid-ocean ridges that are more than 60 times greater than the commonly assumed pelagic burial rate of 0.5 $\mu g\,cm^{-2}\,yr^{-1}$ (Boström et al., 1973), the model value may be too high. For example, end-member hydrothermal fluids with 1 mM Mn (see Supporting Information for hydrothermal data sources) and a high-temperature hydrothermal water flux of 6.5×10^{13} $kg\,yr^{-1}$ (e.g., Elderfield and Schultz, 1996) are more consistent with a *maximum* hydrothermal input of 6.5×10^{10} $mol\,yr^{-1}$ and a required Mn output rate of 1.3 $\mu g\,cm^{-2}\,yr^{-1}$. Fig. 8 also explores solutions for these two Mn burial rates (black versus red curves).

In all models in Fig. 8, Sink 1 represents abyssal pelagic sediments with the Ni/Mn and Ni isotope characteristics outlined above. In panel A, Sink 2 has the geochemical and isotopic characteristics of the California Margin suboxic sediments, with the different curves assigning Ni/Mn ratios to these sediments that cover the observed range. The combined operation of these two sinks cannot reproduce the size and isotope composition of the global Mn oxide sink required by mass balance (the blue rectangle in Fig. 8). They come closest for models with the lower Mn burial rate and the lowest measured Ni/Mn ratio in Sink 2 (0.004). Otherwise too much Ni is buried. Moreover, this mass balance can only be achieved if this suboxic setting covers approximately 60-70% of the ocean floor, which is highly unrealistic. Finally, the models don't work at all for the higher, much more plausible, Mn burial rate. In contrast, the models in panel B, where Sink 2 has the geochemical and isotopic characteristics of proximal hydrothermal sediments,

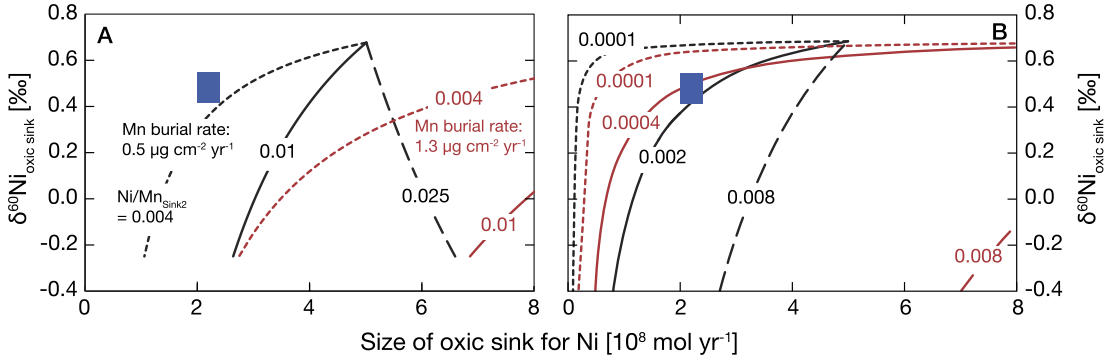

Fig. 8. The size and isotope composition of the global Mn oxide sink for Ni assuming it is partitioned into two different sub-sinks. The two panels show two sets of mixing curves between two end-member sinks of Ni to Mn-rich sediment. In both panels, Sink 1 is to abyssal-pelagic sediment. In panel A, Sink 2 is to sub-oxic sediments such as those of the California Margin. In panel B, Sink 2 is to hydrothermal sediments. In each panel, the black curves are for a low-end estimate of the global Mn burial rate (0.5 µg cm^{-2} yr^{-1}), and the red curves for a high-end estimate (1.3 µg cm^{-2} yr^{-1}). The family of black curves represents low, medium and high estimates of the Ni/Mn ratios for endmember 2, as do the red curves. For both panels, Sink 1 (abyssal pelagic ocean) has a Ni/Mn ratio of 0.02 g/g and a δ^{60}Ni = +0.68±0.24. In panel A, Sink 2 has geochemical characteristics of suboxic sediments such as those of the California Margin, with Ni/Mn = 0.004-0.025 and δ^{60}Ni = -0.25‰. In panel B, Sink 2 has geochemical characteristics of proximal hydrothermal sediments, with Ni/Mn = 0.0001-0.0008 and δ^{60}Ni = -1.06‰. The blue rectangle shows the size and isotope composition of the global Mn oxide sink obtained by overall Ni mass balance (Fig. 1). For models in panel A, the elemental and isotope budgets cannot be balanced together. The closest the models get are with the lower Mn burial rate, with a suboxic sink that has a Ni/Mn at the extreme lower end of the observed range. However, in this case, suboxic sediments are modelled to cover an unrealistic 60-70% of the area of the ocean bottom beneath an oxic water column. Models in panel B resolve the elemental and isotope budgets for both Mn burial rates and for Ni/Mn ratios of Sink 2 that are well within the range measured for hydrothermal sediments.

can easily reproduce the size and isotope composition of the global Mn oxide sink of Ni. For the two different Mn burial rates, this solution is found for a Ni/Mn ratio of Sink 2 of 0.0004 and 0.002, both well within the measured range for proximal hydrothermal sediments. The other important implication is that, because of the different Ni/Mn ratios of the sinks, these solutions require that 50-90% of Mn burial occurs via proximal hydrothermal sediments, but 85-90% of Ni burial occurs via the abyssal pelagic sink.

6. Conclusions

This study presents new Ni concentration and isotope data from fully oxic, Mn-rich abyssal pelagic sediments from 7 different sites across the open Pacific and 10 closely-spaced sites in the Indian Ocean. In addition, it presents data from one hemipelagic site from the suboxic California Margin. Abyssal Pacific and Indian Ocean sediments have a Ni/Mn ratio of 0.02 g/g (similar to Fe-Mn crusts) and their authigenic Ni is isotopically lighter (δ^{60}Ni = +0.26 to +1.08‰) than seawater (+1.33‰) and Fe-Mn crusts (+1.55±0.38‰). The organic carbon-rich suboxic sediments of the Californian margin measured here have lower Ni/Mn ratios (0.004 to 0.014) and even lighter authigenic Ni isotope compositions (δ^{60}Ni = -0.08±0.11‰). The Ni isotopes of nearly all Mn-rich sediments and deposits analysed to date are correlated with Co/Mn ratios, suggesting that both are controlled by accumulation rate, progressive incorporation of Ni into the structure and isotopic re-equilibration between the solid and aqueous phase. At sites where sediments are diagenetically processed, such as the California Margin, differential diagenetic remobilisation of Mn, Ni and Co cause deviations from the above correlation.

In putting forward the new mass balance, we have emphasised the requirement that the final net amount and isotope composition of Ni must balance the inputs from sources external to the ocean. The two key differences between the view of the oceanic Ni budget presented here and those in other recent studies (e.g. Little et al., 2020; Gueguen et al., 2021) are: (1) the realisation that Fe-Mn crusts and nodules are an insignificant part of the Mn output (Uramoto et al., 2019), so that their heavy Ni isotope compositions are an insignificant part of the Ni isotope budget and; (2) the fact that a substantial portion of the Mn oxide sink is associated with a Ni/Mn ratio much less than the 0.02 g/g of most pelagic sediments. The range of Ni isotope compositions observed for marine Mn-rich sediments may simply be explained by removal from the water column, without further diagenetic modification, and with their variable isotope compositions resulting from variation in accumulation rates and the relative importance of sorption versus incorporation. However, we do not rule out the possibility suggested previously (Ciscato et al., 2018; Little et al., 2020; Gueguen and Rouxel, 2021), that the final Ni isotope composition of sediments in some settings is determined by removal of heavier isotopes from the water column close to the abyssal pelagic sediments measured here, followed by diagenetic remobilisation, mineral transformations and a flux of Ni back across the sediment-water interface. Indeed, such loss of Ni appears to be required by porewater data and seems to be the only explanation of the low Ni/Mn ratio of the oxidatively re-precipitated Mn oxide at the sediment-water interface. Nickel isotope measurements of pore waters will be essential in further assessing the isotopic impact of such a process.

CRediT authorship contribution statement

Sarah Fleischmann: Conceptualization, Formal analysis, Investigation, Validation, Visualization, Writing – original draft, Writing – review & editing. **Jianghui Du:** Methodology, Supervision, Visualization, Writing – original draft, Writing – review & editing. **Aditi Chatterjee:** Investigation, Writing – review & editing. **James McManus:** Resources, Writing – original draft, Writing – review & editing. **Sridhar D. Iyer:** Resources, Writing – review & editing. **Ankeeta Amonkar:** Resources, Writing – review & editing. **Derek Vance:** Conceptualization, Formal analysis, Funding acquisition, Investigation, Methodology, Project administration, Supervision, Validation, Visualization, Writing – original draft, Writing – review & editing.

Declaration of competing interest

The authors declare that they have no known competing financial interests or personal relationships that could have appeared to influence the work reported in this paper.

Data availability

All the data presented in this manuscript can be found in the Supporting Information.

Acknowledgements

We thank Alexandra Hangsterfer of the Scripps Institute of Oceanography core collection and Nichole Anest of the Lamont-Doherty core repository for help with obtaining the abyssal Pacific samples. AA and SDI thank Dr. Sunil Kumar Singh, Director CSIR-NIO, Goa for granting permission to work on the Indian Ocean sediment samples. Thanks to Caroline Peacock and Lena Chen for comments on an earlier draft of the paper. This research was supported by Swiss National Science Foundation grant 200021-184873 and the European Union's Horizon 2020 research and innovation programme under Marie Skłodowska-Curie grant agreement 891489. We are very grateful to editor Laurence Coogan for pointing us in the direction of hydrothermal Ni data, also helped by discussions with Gretchen Früh-Green. We also thank Laura Wasylenki and an anonymous reviewer for comments that helped us to significantly clarify and improve the manuscript.

Appendix A. Supplementary material

Supplementary material related to this article can be found online at https://doi.org/10.1016/j.epsl.2023.118301.

References

Amonkar, A., Iyer, S.D., 2021. Influence of low-temperature and post-depositional changes in the siliceous-pelagic sediments of the Central Indian Ocean Basin. J. Sediment. Environ. 6, 603–620. https://doi.org/10.1007/s43217-021-00073-4.

Archer, C., Vance, D., Milne, A., Lohan, M.C., 2020. The oceanic biogeochemistry of nickel and its isotopes: new data from the South Atlantic and the Southern Ocean biogeochemical divide. Earth Planet. Sci. Lett. 535, 116118. https://doi.org/10.1016/j.epsl.2020.116118.

Atkins, A.L., Shaw, S., Peacock, C.L., 2014. Nucleation and growth of todorokite from birnessite: implications for trace-metal cycling in marine sediments. Geochim. Cosmochim. Acta 144, 109–125. https://doi.org/10.1016/j.gca.2014.08.014.

Atkins, A.L., Shaw, S., Peacock, C.L., 2016. Release of Ni from birnessite during transformation of birnessite to todorokite: implications for Ni cycling in marine sediments. Geochim. Cosmochim. Acta 189, 158–183. https://doi.org/10.1016/j.gca.2016.06.007.

Berelson, W.M., McManus, J., Coale, K.H., Johnson, K.S., Kilgore, T., Burdige, D., Pilskaln, C., 1996. Biogenic matter diagenesis on the sea floor: a comparison between two continental margin transects. J. Mar. Res. 54 (4), 731–762. https://doi.org/10.1357/0022240963213673.

Bertram, C.J., Elderfield, H., 1993. The geochemical balance of the rare earth elements and neodymium isotopes in the oceans. Geochim. Cosmochim. Acta 57 (9), 1957–1986. https://doi.org/10.1016/0016-7037(93)90087-D.

Böning, P., Shaw, T., Pahnke, K., Brumsack, H.J., 2015. Nickel as indicator of fresh organic matter in upwelling sediments. Geochim. Cosmochim. Acta 162, 99–108. https://doi.org/10.1016/j.gca.2015.04.027.

Böning, P., Fröllje, H., Beck, M., Schnetger, B., Brumsack, H.J., 2012. Underestimation of the authigenic fraction of Cu and Ni in organic-rich sediments. Mar. Geol. 323, 24–28. https://doi.org/10.1016/j.margeo.2012.07.004.

Boström, K., Kraemer, T., Gartner, S., 1973. Provenance and accumulation rates of opaline silica, Al, Ti, Fe, Mn, Cu, Ni and Co in Pacific pelagic sediments. Chem. Geol. 11 (2), 123–148. https://doi.org/10.1016/0009-2541(73)90049-1.

Bruland, K.W., 1980. Oceanographic distributions of cadmium, zinc, nickel, and copper in the North Pacific. Earth Planet. Sci. Lett. 47 (2), 176–198. https://doi.org/10.1016/0012-821X(80)90035-7.

Burns, R.G., Burns, V.M., 1977. Mineralogy. In: Glasby, G.P. (Ed.), Marine Manganese Deposits. In: Elsevier Oceanography Series, vol. 15, pp. 185–248.

Cameron, V., Vance, D., 2014. Heavy nickel isotope compositions in rivers and the oceans. Geochim. Cosmochim. Acta 128, 195–211. https://doi.org/10.1016/j.gca.2013.12.007.

Cameron, V., Vance, D., Archer, C., House, C.H., 2009. A biomarker based on the stable isotopes of nickel. Proc. Natl. Acad. Sci. USA 106 (27), 10944–10948. https://doi.org/10.1073/pnas.0900726106.

Chen, L., Archer, C., Little, S.H., Peacock, C.L., 2022. An isotopically heavy source of nickel: release of nickel during birnessite transformation into todorokite. In: Goldschmidt Conference 2022.

Ciscato, E.R., Bontognali, T.R., Vance, D., 2018. Nickel and its isotopes in organic-rich sediments: implications for oceanic budgets and a potential record of ancient seawater. Earth Planet. Sci. Lett. 494, 239–250. https://doi.org/10.1016/j.epsl.2018.04.061.

Corliss, J.B., Lyle, M., Dymond, J., Crane, K., 1978. The chemistry of hydrothermal mounds near the Galapagos Rift. Earth Planet. Sci. Lett. 40 (1), 12–24. https://doi.org/10.1016/0012-821X(78)90070-5.

D'Hondt, S., Inagaki, F., Zarikian, C.A., Abrams, L.J., Dubois, N., Engelhardt, T., Evans, H., Ferdelman, T., Gribshol, B., Harris, R.N., Hoppie, B.W., Hyun, J., Kallmeyer, J., Kim, J., Lynch, J.E., McKinley, C.C., Mitsunobu, S., Morono, Y., Murray, R.W., Ziebis, W., 2015. Presence of oxygen and aerobic communities from sea floor to basement in deep-sea sediments. Nat. Geosci. 8 (4), 299–304. https://doi.org/10.1038/ngeo2387.

Edmond, J.M., Measures, C., Mangum, B., Grant, B., Sclater, F.R., Collier, R., Hudson, A., Gordon, L.I., Corliss, J.B., 1979. On the formation of metal-rich deposits at ridge crests. Earth Planet. Sci. Lett. 46 (1), 19–30. https://doi.org/10.1016/0012-821X(79)90062-1.

Elderfield, H., 1976. Manganese fluxes to the oceans. Mar. Chem. 4 (2), 103–132. https://doi.org/10.1016/0304-4203(76)90001-3.

Elderfield, H., Schultz, A., 1996. Mid-ocean ridge hydrothermal fluxes and the chemical composition of the ocean. Annu. Rev. Earth Planet. Sci. 24 (1), 191–224. https://doi.org/10.1146/annurev.earth.24.1.191.

Finney, B.P., Lyle, M.W., Heath, G.R., 1988. Sedimentation at MANOP Site H (eastern equatorial Pacific) over the past 400,000 years: climatically induced redox variations and their effects on transition metal cycling. Paleoceanography 3 (2), 169–189. https://doi.org/10.1029/PA003i002p00169.

Gall, L., Williams, H.M., Siebert, C., Halliday, A.N., Herrington, R.J., Hein, J.R., 2013. Nickel isotopic compositions of ferromanganese crusts and the constancy of deep ocean inputs and continental weathering effects over the Cenozoic. Earth Planet. Sci. Lett. 375, 148–155. https://doi.org/10.1016/j.epsl.2013.05.019.

Gueguen, B., Rouxel, O., 2021. The Nickel isotope composition of the authigenic sink and the diagenetic flux in modern oceans. Chem. Geol. 563, 120050. https://doi.org/10.1016/j.chemgeo.2020.120050.

Gueguen, B., Rouxel, O., Fouquet, Y., 2021. Nickel isotopes and rare earth elements systematics in marine hydrogenetic and hydrothermal ferromanganese deposits. Chem. Geol. 560, 119999. https://doi.org/10.1016/j.chemgeo.2020.119999.

Gueguen, B., Rouxel, O., Rouget, M.L., Bollinger, C., Ponzevera, E., Germain, Y., Fouquet, Y., 2016. Comparative geochemistry of four ferromanganese crusts from the Pacific Ocean and significance for the use of Ni isotopes as paleoceanographic tracers. Geochim. Cosmochim. Acta 189, 214–235. https://doi.org/10.1016/j.gca.2016.06.005.

Gueguen, B., Sorensen, J.V., Lalonde, S.V., Peña, J., Toner, B.M., Rouxel, O., 2018. Variable Ni isotope fractionation between Fe-oxyhydroxides and implications for the use of Ni isotopes as geochemical tracers. Chem. Geol. 481, 38–52. https://doi.org/10.1016/j.chemgeo.2018.01.023.

Halbach, P., Segl, M., Puteanus, D., Mangini, A., 1983. Co-fluxes and growth rates in ferromanganese deposits from central Pacific seamount areas. Nature 304 (5928), 716–719. https://doi.org/10.1038/304716a0.

He, Z., Archer, C., Yang, S., Vance, D., 2023. Sedimentary cycling of zinc and nickel and their isotopes on an upwelling margin: implications for oceanic budgets and paleoenvironment proxies. Geochim. Cosmochim. Acta 343, 84–97. https://doi.org/10.1016/j.gca.2022.12.026.

Hein, J.R., Koschinsky, A., Bau, M., Manheim, F.T., Kang, J.K., Roberts, L., 2000. Cobalt-rich ferromanganese crusts in the Pacific. In: Cronan, D.S. (Ed.), Handbook of Marine Mineral Deposits, pp. 239–279.

Heller, C., Kuhn, T., Versteegh, G.J., Wegorzewski, A.V., Kasten, S., 2018. The geochemical behavior of metals during early diagenetic alteration of buried manganese nodules. Deep-Sea Res., Part 1 142, 16–33. https://doi.org/10.1016/j.dsr.2018.09.008.

John, S.G., Kelly, R.L., Bian, X., Fu, F., Smith, M.I., Lanning, N.T., Liang, H., Pasquier, B., Seelen, E.A., Holzer, M., Wasylenki, L., Conway, T.M., Fitzsimmons, J.N., Hutchins, D.A., Yang, S.C., 2022. The biogeochemical balance of oceanic nickel cycling. Nat. Geosci. 15 (11), 906–912. https://doi.org/10.1038/s41561-022-01045-7.

Koschinsky, A., Halbach, P., 1995. Sequential leaching of marine ferromanganese precipitates: genetic implications. Geochim. Cosmochim. Acta 59 (24), 5113–5132. https://doi.org/10.1016/0016-7037(95)00358-4.

Kraemer, T., Schornick, J.C., 1974. Comparison of elemental accumulation rates between ferromanganese deposits and sediments in the South Pacific Ocean. Chem. Geol. 13 (3), 187–196. https://doi.org/10.1016/0009-2541(74)90019-9.

Krishnaswami, S., 1976. Authigenic transition elements in Pacific pelagic clays. Geochim. Cosmochim. Acta 40 (4), 425–434. https://doi.org/10.1016/0016-7037(76)90007-7.

Kwon, K.D., Refson, K., Sposito, G., 2013. Understanding the trends in transition metal sorption by vacancy sites in birnessite. Geochim. Cosmochim. Acta 101, 222–232. https://doi.org/10.1016/j.gca.2012.08.038.

Lauvset, S.K., Lange, N., Tanhua, T., Bittig, H.C., Olsen, A., Kozyr, A., Alin, S., Álvarez, M., Kumiko, A., Barbero, L., Becker, S., Brown, P.J., Carter, B.R., Cotrim da Cunha, L., Feely, R.A., Hoppema, M., Humphreys, M.P., Ishii, M., Jeansson, E., Jiang, L., Jones, S.D., Lo Monaco, C., Murata, A., Müller, J.D., Pérez, F.F., Pfeil, B., Schirnick, C., Steinfeldt, R., Suzuki, T., Tilbrook, B., Ulfsbo, A., Velo, A., Woosely, R.J., Key, R.M., 2022. GLODAPv2.2022: the latest version of the global interior ocean biogeochemical data product. Earth Syst. Sci. Data Discuss. 14 (12), 5543–5572. https://doi.org/10.5194/essd-14-5543-2022.

Lemaitre, N., Du, J., de Souza, G.F., Archer, C., Vance, D., 2022. The essential bioactive role of nickel in the oceans: evidence from nickel isotopes. Earth Planet. Sci. Lett. 584, 117513. https://doi.org/10.1016/j.epsl.2022.117513.

Little, S.H., Archer, C., McManus, J., Najorka, J., Wegorzewski, A.V., Vance, D., 2020. Towards balancing the oceanic Ni budget. Earth Planet. Sci. Lett. 547, 116461. https://doi.org/10.1016/j.epsl.2020.116461.

Lyle, M., Heath, G.R., Robbins, J.M., 1984. Transport and release of transition elements during early diagenesis: sequential leaching of sediments from MANOP Sites M and H. Part I. pH 5 acetic acid leach. Geochim. Cosmochim. Acta 48 (9), 1705–1715. https://doi.org/10.1016/0016-7037(84)90026-7.

Mackey, D.J., O'Sullivan, J.E., Watson, R.J., Dal Pont, G., 2002. Trace metals in the Western Pacific: temporal and spatial variability in the concentrations of Cd, Cu, Mn and Ni. Deep-Sea Res., Part 1 49 (12), 2241–2259. https://doi.org/10.1016/S0967-0637(02)00124-3.

Manceau, A., Lanson, M., Geoffroy, N., 2007. Natural speciation of Ni, Zn, Ba, and As in ferromanganese coatings on quartz using X-ray fluorescence, absorption, and diffraction. Geochim. Cosmochim. Acta 71 (1), 95–128. https://doi.org/10.1016/j.gca.2006.08.036.

Manheim, F.T., Lane-Bostwick, C.M., 1988. Cobalt in ferromanganese crusts as a monitor of hydrothermal discharge on the Pacific sea floor. Nature 335 (6185), 59–62. https://doi.org/10.1038/335059a0.

Manheim, F.T., Lane-Bostwick, C.M., 1989. Chemical composition of ferromanganese crusts in the world ocean: a review and comprehensive database. Open-File Report 89-020. U.S. Geological Survey, Woods Hole, MA.

McManus, J., Berelson, W.M., Coale, K.H., Johnson, K.S., Kilgore, T.E., 1997. Phosphorus regeneration in continental margin sediments. Geochim. Cosmochim. Acta 61 (14), 2891–2907. https://doi.org/10.1016/S0016-7037(97)00138-5.

McManus, J., Berelson, W.M., Severmann, S., Johnson, K.S., Hammond, D.E., Roy, M., Coale, K.H., 2012. Benthic manganese fluxes along the Oregon–California continental shelf and slope. Cont. Shelf Res. 43, 71–85. https://doi.org/10.1016/j.csr.2012.04.016.

McMurtry, G.M., 2009. Authigenic deposits. In: Steele, J.H., Thorpe, S.A., Turekian, K.K. (Eds.), Marine Chemistry & Geochemistry: A Derivative of the Encyclopedia of Ocean Sciences, second ed. Elsevier, Oxford, pp. 325–335.

Nozaki, Y., Alibo, D.S., Amakawa, H., Gamo, T., Hasumoto, H., 1999. Dissolved rare earth elements and hydrography in the Sulu Sea. Geochim. Cosmochim. Acta 63 (15), 2171–2181. https://doi.org/10.1016/S0016-7037(99)00142-8.

Peacock, C.L., 2009. Physiochemical controls on the crystal-chemistry of Ni in birnessite: genetic implications for ferromanganese precipitates. Geochim. Cosmochim. Acta 73 (12), 3568–3578. https://doi.org/10.1016/j.gca.2009.03.020.

Peacock, C.L., Sherman, D.M., 2007. Crystal-chemistry of Ni in marine ferromanganese crusts and nodules. Am. Mineral. 92 (7), 1087–1092. https://doi.org/10.2138/am.2007.2378.

Plass, A., Dale, A.W., Scholz, F., 2021. Sedimentary cycling and benthic fluxes of manganese, cobalt, nickel, copper, zinc and cadmium in the Peruvian oxygen minimum zone. Mar. Chem. 233, 103982. https://doi.org/10.1016/j.marchem.2021.103982.

Ragsdale, S.W., 2009. Nickel-based enzyme systems. J. Biol. Chem. 284 (28), 18571–18575. https://doi.org/10.1074/jbc.R900020200.

Rehkämper, M., Nielsen, S.G., 2004. The mass balance of dissolved thallium in the oceans. Mar. Chem. 85 (3–4), 125–139. https://doi.org/10.1016/j.marchem.2003.09.006.

Reinhard, C.T., Planavsky, N.J., Robbins, L.J., Partin, C.A., Gill, B.C., Lalonde, S.V., Bekker, A., Konhauser, K.O., Lyons, T.W., 2013. Proterozoic ocean redox and biogeochemical stasis. Proc. Natl. Acad. Sci. USA 110 (14), 5357–5362. https://doi.org/10.1073/pnas.120862211.

Rudnick, R.L., Gao, S., 2014. Composition of the continental crust. In: Holland, H.D., Turekian, K.K. (Eds.), Treatise on Geochemistry, vol. 4, second edition, pp. 1–51.

Saunders, N.J., Barling, J., Harvey, J., Halliday, A.N., 2020. Heterogeneous nickel isotopic compositions in the terrestrial mantle–part 1: ultramafic lithologies. Geochim. Cosmochim. Acta 285, 129–149. https://doi.org/10.1016/j.gca.2020.06.029.

Sawlan, J.J., Murray, J.W., 1983. Trace metal remobilization in the interstitial waters of red clay and hemipelagic marine sediments. Earth Planet. Sci. Lett. 64 (2), 213–230. https://doi.org/10.1016/0012-821X(83)90205-4.

Schmidt, K., Garbe-Schönberg, D., Hannington, M.D., Anderson, M.O., Bühring, B., Haase, K., Haruel, C., Lupton, J., Koschinsky, A., 2017. Boiling vapour-type fluids from the Nifonea vent field (New Hebrides Back-Arc, Vanuatu, SW Pacific): geochemistry of an early-stage, post-eruptive hydrothermal system. Geochim. Cosmochim. Acta 207, 185–209. https://doi.org/10.1016/j.gca.2017.03.016.

Sclater, F.R., Boyle, E., Edmond, J.M., 1976. On the marine geochemistry of nickel. Earth Planet. Sci. Lett. 31 (1), 119–128. https://doi.org/10.1016/0012-821X(76)90103-5.

Scott, C., Lyons, T.W., Bekker, A., Shen, Y.A., Poulton, S.W., Chu, X.L., Anbar, A.D., 2008. Tracing the stepwise oxygenation of the Proterozoic ocean. Nature 452 (7186), 456–459. https://doi.org/10.1038/nature06811.

Shaw, T.J., Gieskes, J.M., Jahnke, R.A., 1990. Early diagenesis in differing depositional environments: the response of transition metals in pore water. Geochim. Cosmochim. Acta 54 (5), 1233–1246. https://doi.org/10.1016/0016-7037(90)90149-F.

Sholkovitz, E.R., Landing, W.M., Lewis, B.L., 1994. Ocean particle chemistry: the fractionation of rare earth elements between suspended particles and seawater. Geochim. Cosmochim. Acta 58 (6), 1567–1579. https://doi.org/10.1016/0016-7037(94)90559-2.

Sorensen, J.V., Gueguen, B., Stewart, B.D., Peña, J., Rouxel, O., Toner, B.M., 2020. Large nickel isotope fractionation caused by surface complexation reactions with hexagonal birnessite. Chem. Geol. 537, 119481. https://doi.org/10.1016/j.chemgeo.2020.119481.

Tagliabue, A., Hawco, N.J., Bundy, R.M., Landing, W.M., Milne, A., Morton, P.L., Saito, M.A., 2018. The role of external inputs and internal cycling in shaping the global ocean cobalt distribution: insights from the first cobalt biogeochemical model. Glob. Biogeochem. Cycles 32 (4), 594–616. https://doi.org/10.1002/2017GB005830.

Uramoto, G.I., Morono, Y., Tomioka, N., Wakaki, S., Nakada, R., Wagai, R., Uesugi, K., Takeuchi, A., Hoshino, M., Suzuki, Y., Shiraishi, F., Mitsunobu, S., Suga, H., Takeichi, Y., Takahashi, Y., Inagaki, F., 2019. Significant contribution of subseafloor microparticles to the global manganese budget. Nat. Commun. 10 (1), 1–10. https://doi.org/10.1038/s41467-019-08347-2.

van Hulten, M., Middag, R., Dutay, J.C., De Baar, H., Roy-Barman, M., Gehlen, M., Tagliabue, A., Sterl, A., 2017. Manganese in the West Atlantic Ocean in the context of the first global ocean circulation model of manganese. Biogeosciences 14 (5), 1123–1152. https://doi.org/10.5194/bg-14-1123-2017.

Vance, D., Little, S.H., Archer, C., Cameron, V., Andersen, M.B., Rijkenberg, M.J., Lyons, T.W., 2016. The oceanic budgets of nickel and zinc isotopes: the importance of sulfidic environments as illustrated by the Black Sea. Philos. Trans. R. Soc. Lond. Ser. A 374 (2081), 20150294. https://doi.org/10.1098/rsta.2015.0294.

Von Damm, K.L., Edmond, J.M., Grant, B., Measures, C.I., Walden, B., Weiss, R.F., 1985. Chemistry of submarine hydrothermal solutions at 21°N, East Pacific Rise. Geochim. Cosmochim. Acta 49 (11), 2197–2220. https://doi.org/10.1016/0016-7037(85)90222-4.

Wang, S.J., Rudnick, R.L., Gaschnig, R.M., Wang, H., Wasylenki, L.E., 2019. Methanogenesis sustained by sulfide weathering during the Great Oxidation Event. Nat. Geosci. 12, 296–300. https://doi.org/10.1038/s41561-019-0320-z.

Wegorzewski, A.V., Grangeon, S., Webb, S.M., Heller, C., Kuhn, T., 2020. Mineralogical transformations in polymetallic nodules and the change of Ni, Cu and Co crystal-chemistry upon burial in sediments. Geochim. Cosmochim. Acta 282, 19–37. https://doi.org/10.1016/j.gca.2020.04.012.